HAL
open science

On the impact of fuel injection angle in Euler–Lagrange large eddy simulations of swirling spray flames exhibiting thermoacoustic instabilities

Ermanno Lo Schiavo, Davide Laera, Eleonore Riber, Laurent Y.M. Gicquel, Thierry Poinsot

To cite this version:

Ermanno Lo Schiavo, Davide Laera, Eleonore Riber, Laurent Y.M. Gicquel, Thierry Poinsot. On the impact of fuel injection angle in Euler–Lagrange large eddy simulations of swirling spray flames exhibiting thermoacoustic instabilities. Combustion and Flame, 2021, 227, pp.359-370. 10.1016/j.combustflame.2021.01.009 . hal-03345242

HAL Id: hal-03345242

https://hal.science/hal-03345242v1

Submitted on 15 Sep 2021

HAL is a multi-disciplinary open access archive for the deposit and dissemination of scientific research documents, whether they are published or not. The documents may come from teaching and research institutions in France or abroad, or from public or private research centers.

L'archive ouverte pluridisciplinaire **HAL**, est destinée au dépôt et à la diffusion de documents scientifiques de niveau recherche, publiés ou non, émanant des établissements d'enseignement et de recherche français ou étrangers, des laboratoires publics ou privés.

Open Archive Toulouse Archive Ouverte

OATAO is an open access repository that collects the work of Toulouse researchers and makes it freely available over the web where possible

This is an author's version published in: https://oatao.univ-toulouse.fr/27453

Official URL:

https://doi.org/10.1016/j.combustflame.2021.01.009

To cite this version:

Lo Schiavo, E.rmanno and Laera, Davide and Riber, Eleonore and Gicquel, Laurent Y.M. and Poinsot, Thierry *On the impact of fuel injection angle in Euler–Lagrange large eddy simulations of swirling spray flames exhibiting thermoacoustic instabilities.* (2021) Combustion and Flame, 227. 359-370. ISSN 0010-2180.

Any correspondence concerning this service should be sent to the repository administrator: tech-oatao@listes-diff.inp-toulouse.fr

On the impact of fuel injection angle in Euler-Lagrange Large Eddy Simulations of swirling spray flames exhibiting thermoacoustic instabilities

E. Lo Schiavo[a], D. Laera[a,*], E. Riber[a], L. Gicquel[a], T. Poinsot[b]

[a] *CERFACS, 42 avenue Gaspard Coriolis, 31057 Toulouse, France*
[b] *Institut de Mécanique des Fluides de Toulouse, IMFT, Université de Toulouse, CNRS, 31400 Toulouse, France*

Abstract

This study deals with the fundamental problem of combustion dynamics in gas turbine combustors operating with liquid fuel. In this framework the present work proposes the study of an academic liquid fueled combustor sensitive to thermoacoustic instabilities, simulated via high-fidelity Large Eddy Simulations. The experimental setup addressed is SICCA-spray from EM2C laboratory featuring both stable and unstable flames depending on the combustion chamber length. The proposed analysis, based on the Euler-Lagrange modeling approach, studies the impact of the spray injection angle θ on both the stable flame and the triggering of the longitudinal combustor acoustic mode when using a longer quartz tube. For the liquid injection modeling, the FIM-UR semi-empirical model is adopted with three different θ values: $\theta = 35°$, $45°$ and $60°$. In stable conditions, the spray angle is proven to have a negligible impact on the flame anchoring point, however, the mean flame length and fuel distribution are found to be slightly modified by the velocity at which droplets enter the combustion chamber. For the thermoacoustically unstable conditions, two well-established stable limit cycles with the same frequency and similar amplitudes are obtained when fuel is injected at $\theta = 45°$ and $60°$. Contrarily, the system stabilizes when $\theta = 35°$ pointing to the importance of the dynamics of the liquid film layer formed inside the injector for this setup. Likewise, this liquid film layer dynamics and its modeling appear critical as already suggested by previous studies on the same configuration. The detailed analysis of the thermoacoustically unstable different predictions is then performed through the investigation of the spatial fields of the local Rayleigh index obtained following the novel extension in the frequency domain of the Rayleigh criterion complemented by the application of Dynamic Mode Decomposition. It confirms that the injection angle of the liquid spray has a significant effect on the thermoacoustic response of the system. Indeed the influence of θ on the dynamics of the liquid fuel when entering the combustion chamber is proven to have an impact on the synchronization mechanism governing the liquid phase with respect to acoustics sustaining the observed limit cycles. More specifically, couplings at the liquid phase level are evidenced by introducing two novel indices correlating the fluctuations of liquid fuel volume fraction and evaporation rate with pressure.

Keywords:
Thermoacoustic instabilities, Turbulent spray flames, Large Eddy Simulations, Spray angle sensitivity, Eulerian-Lagrangian approach

1. Introduction

The investigation of thermoacoustic instabilities has driven multiple studies around modern gas turbine engines in the past two decades [1]. In the prediction tool developing scenario, notwithstanding the availability of lower cost tools such as analytical models or low-order models [2, 3], the appeal of Large Eddy Simulations (LES) is increasing for industrial use, given their higher accurate prediction capabilities [4, 5]. In this context, much of the efforts concerned instabilities arising in combustors operating in gaseous premixed or partially premixed mode. A much smaller group of studies deals with cases where the fuel is injected as a liquid spray, as in the next generation of aero-engines [6], for which addressing the modeling of multiphase flow is still a great challenge. To tackle this problem, the liquid fuel can be resolved with an Eulerian formulation [7] (EE), or by tracking droplet trajectories individually as done in the Lagrangian approach [8] (EL). In the framework of combustion dynamics, both approaches have been applied [9–11] and the importance of reproducing accurately the spray properties like the droplet size distribution have been shown to be a key aspect since it participates to the feedback loop between flame and acoustics [12, 13]. However, none of these numerical studies takes into account possible variations at the injection system level. From an experimental point of view, studies are mainly centred on the impact of injecting an oscillating fuel mass flow rate. Giuliani *et al.* [14] proposed one of the first characterization of the fuel spray issued from an airblast atomizer when the air and liquid supplies are pulsed by a sinusoidal signal representing the effect of a thermoacoustic limit cycle. Local spray density and flame position were observed fluctuating in phase with the imposed modulation. The complete characterisation of the flame transfer functions to liquid-fuel modulation was more recently accomplished by Yi and Santavicca [15]. Due to the

*Corresponding author: laera@cerfacs.fr

simplicity of the injection system consisting in a single point fuel nozzle, variation of the injection spray angle was not possible in their configuration. For internal combustion engine applications, this was accomplished by Fang *et al.* [16] and Wang *et al.* [17] who investigated the impact of injection angles and injection pressures on the steady combustion process and pollutant emissions. Starting from their results, a similar study can be imagined also in a gas turbine system. In most gas turbine applications, pressure-swirled atomizers are usually adopted so the liquid is injected as a swirling hollow cone spray. In such systems, the liquid injection is usually located inside the combustor, i.e., in places lacking of an optic access which makes the direct measurements of the angle of the injected spray not possible. From a numerical point of view, the atomization process of a pressure-swirled atomizer is usually described making use of some empirical correlations [18]. If a given mass flow rate, $\dot{m}_\ell$, is assumed to be injected in the system, a discharge coefficient C_D could be defined as inversely proportional to the square root of the liquid line pressure drop Δp_ℓ and the discharge orifice surface A_0: $C_D = \dot{m}_\ell / A_0 \sqrt{2\rho_l \Delta p_\ell}$ where ρ_l is the liquid density. From experiments [19], it is well know that the angle at which the spray is injected is a function of this discharge coefficient. Relying on these correlations, injection models defining the velocities at which the liquid particles are injected could be formulated, e.g., see the FIM-UR model used in this work [20]. Clearly, variations in the operating conditions, like the pressure drop, or in fuel properties, will have an impact on the resulting spray angle [21]. In addition to the variability due to uncertainties, it should be stressed that in gas turbines the atomizer is not operated in still air but, usually, a swirled flow interacts with the injected liquid fuel with the objective to improve the breakup and mixing process. As a consequence, the interaction with the swirled gas may have a determinant impact on the spray properties of a single atomizer independently of the fuel mass flow rate it operates with, i.e. the radial and tangential components of shear stresses may lead to abrupt breakdown of the liquid column (known as "explosive breakup") when reaching a critical level [22–24].

Based on these considerations, the present work aims at providing the importance of the spray injection specification via high-fidelity LES-EL performed for the SICCA-spray combustor developed at the EM2C laboratory, CNRS (CentraleSupélec, Paris, France) which features a swirled spray flame fueled by a simplex atomizer [25]. The setup was selected for the current study for multiple reasons:

- the combustor presents either a stable flame or a self-sustained limit cycle depending on the length of the flame tube with which it is operated [26, 27]. The SICCA-spray is therefore a unique system where the impact of spray property variations can be investigated on both operative regimes.

- The effective spray opening angle during the two previously mentioned operative conditions is unkown since "explosive breakup" of the liquid jet have been observed in recent PDA measurements performed at EM2C [24].

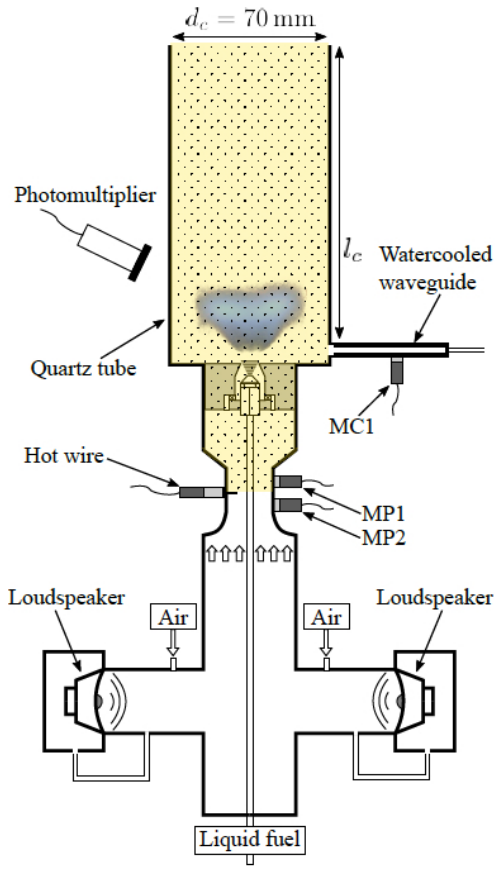

Figure 1: A schematic of the SICCA-spray combustor [26] with the portion considered for the LES highlighted in yellow.

- Finally, the same authors performed previous LES studies of the same system [28, 29] revealing the coupling mechanism between the acoustic mode and the liquid film forming on the injector walls to be fundamental to trigger and sustain the thermoacoustic limit cycle. This conclusion however questions the impact of an injection angle variation which is expected to modify the liquid film and therefore its coupling with the thermoacoustic mode.

In the present work, the SICCA-spray rig is computed assuming three different injection spray angles starting from the results of [28] with the objective of probing their sensitivity to modeling features while deciphering the leading phenomenological process at the origin of the observed thermoacoustic instabilities in swirled liquid-fueled flames. The article is organised as follows: starting with the description of the numerical models in section 2, in section 3 results are discussed starting from the stable flame, section 3.1, followed by the limit cycle condition in section 3.2.

2. Numerical and experimental setup

The SICCA-spray, displayed in Fig. 1 [26], comprises a longitudinal plenum coupled to a quartz flame tube by a radial

swirler. Liquid n-heptane is used in this study and it is injected after the swirler and upstream the combustion chamber through a pressure-swirl atomizer. Experimentally, a stable flame is experienced with chambers shorter than a threshold value, above which a well established self-sustained limit cycle coupled with the first longitudinal mode of the flame tube is observed [27]. During the limit cycle, pressure fluctuations are recorded by a pressure tap located at the backplane of the combustion chamber and the transparent chamber wall allows optical access to the flame dynamics [25].

The numerical domain (highlighted in yellow in Fig. 1) and the modelling strategies used in the present LES are unchanged with respect to the previous studies. A detailed description of the numerical approach can therefore be found in Ref. [28] and only key elements are recalled hereafter. Two different flame tubes of length $\ell_c^{(1)} = 165\,\text{mm}$ and $\ell_c^{(2)} = 280\,\text{mm}$ are adopted for the non-oscillating and oscillating cases, respectively, as in the experiments. The domain is discretized by approximately 20M tetrahedral elements designed with a refinement of $\Delta x \simeq 150\,\mu\text{m}$ in the finest region positioned at the flame root while $\Delta x \simeq 200 - 300\,\mu\text{m}$ is used further downstream. For the simulations, the code AVBP developed by CERFACS (http://www.cerfacs.fr/avbp7x) solving the LES-filtered compressible Navier-Stokes equations is employed making use of the WALE model [30] for turbulent closure. The third order accurate Taylor-Galerkin scheme [31] is adopted together with Navier-Stokes Characteristic Boundary Condition (NSCBC) treatments [32] for inlets and outlets imposing the air mass flow rate with a turbulent mean profile and ambient pressure, respectively. Adiabatic non-slip walls are applied elsewhere aside from the quartz tube and chamber backplane where heat losses are taken into account through a heat resistance and temperature values matching the experimental measurements. Chemical reaction is described by a global two-step six-species scheme $2S_C7H16_DP$ with Pre-Exponential Adjustment (PEA) function [33]. Turbulent combustion is modelled using the two-phase flame extension of the dynamic thickened flame model (TP-TFLES) [33]. These flames are usually characterised by both premix and diffusion combustion regimes [28], so in order to guarantee a proper application of the thickened flame model, which is correctly defined only for premixed flames, an additional conditioning is applied using the Takeno flame index (FI) [34] classically defined as a function of the gradient of fuel and oxidizer mass fractions: $FI = \nabla Y_{C_7H_{16}} \cdot \nabla Y_{O_2} / |\nabla Y_{C_7H_{16}} \cdot \nabla Y_{O_2}|$.

The liquid phase is modeled using a Lagrangian approach. The Schiller-Naumann correlation and the Abramzon and Sirignano model [35] describe drag and evaporation, respectively. The operating conditions prescribe a global ratio of $\phi_{gas} = 0.85$ imposed by the air mass flow rate of $\dot{m}_{air} = 2.58\,\text{g/s}$ at the hot wire location and $\dot{m}_\ell = 0.144\,\text{g/s}$ for the liquid fuel. Droplets are injected through a flat annulus positioned at the atomizer location using the FIM-UR model [20] It treats the injection of a hollow cone spray resulting from a simplex atomizer in which the axial and tangential components of injected liquid droplets velocity are formulated as a function of the fuel mass flow rate $\dot{m}_\ell$ and injection half-cone spray angle θ. Three values of this angle are assumed to perform the sensitivity analysis: $\theta = 35°$ (case A), $\theta = 45°$ (case B) and $\theta = 60°$ (case C). Case B is the same condition computed in Ref. [28] and will be used as reference.

Finally, it is worth mentioning that, following previous works on the same configuration [28, 29], the droplet size distribution is imposed via a *Rosin-Rammler* probability density function (PDF) fitted from experimental measurements of mean (D_{10}) and Sauter diameters (SMD or D_{32}) taken at $z = 2.5$ mm in the combustion chamber: $D_{10} = 10\,\mu\text{m}$ and $D_{32} = 18\,\mu\text{m}$. Since the primary objective is to investigate only the effect of the spray angle, changes in terms of droplet diameter are only due to evaporation, neglecting phenomena like primary and secondary atomization as well as splash and liquid film break-up at the edge of the injector wall. When it comes to particle-wall interaction, it is modeled using Saint-Venant equations for non-evaporating liquid film layers as in [36].

3. Results and Discussion

3.1. Steady flame

First, the thermoacoustically stable condition is studied. A validation of the velocity profiles and injector head losses in non-reacting conditions is proposed in [28]. In the present work, LES results are analysed comparing the three different fuel injection angles. A particular attention is given to the resulting dynamics of the liquid phase in the combustion chamber as well as the implications on the mean flame shape and combustion regimes, i.e., all features that are known to be crucial to determine a burner thermoacoustic stability.

The instantaneous spatial distribution of droplet diameters, displayed in Fig. 2-(bottom row), shows the effect of a wider injection angle inside the injector. Augmenting θ increases the amount of fuel involved in a liquid wall interaction process and, indeed, as the liquid hollow cone widens from 35° (case A) to 60° (case C), the point where the spray impinges the injector wall clearly changes. In case A, this interaction point is almost at the injector edge so a large amount of droplets enters the combustion chamber straight from the injection point. For $\theta = 60°$ (case C), instead, all injected droplets hit the outer cone of the injector before entering the combustion chamber. Therefore, in this case, the dynamics of the liquid film layer forming on the injector wall is entirely responsible for the spatial droplet distribution further downstream whereas this is not happening with the smaller injection angle. Note however that the effect of the droplet dynamics on the gaseous flow is negligible as shown in Fig. 2-(top row). The same flow structure can be observed in the three cases in terms of both central recirculation zone (CRZ), shear layer position and strength, as highlighted by the black line corresponding to the axial gaseous velocity of $U_{g,z} = 15\,\text{m/s}$.

The major effect of the presence of a liquid film on the wall is to decrease the axial momentum of the liquid n-heptane droplets entering the combustion chamber. Indeed, when the liquid fuel generates a film layer, the droplet original momentum imposed at injection is lost in favour of a locally averaged film velocity which is a function of the local shear stress

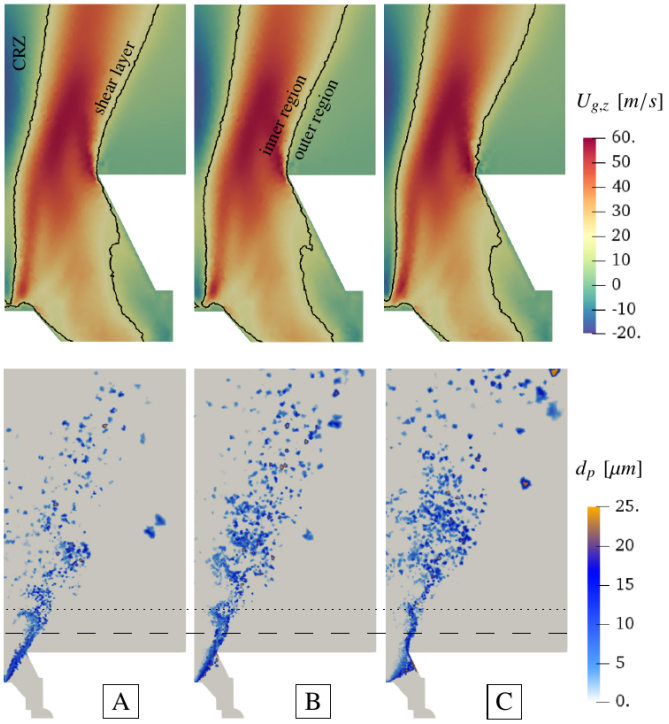

Figure 2: Mean gaseous axial velocity field zoomed on the injector region (top row) and instantaneous snapshot of droplet diameter distribution within the combustor (bottom row) in the three cases: $\theta = 35°$ (case A), $\theta = 45°$ (case B) and $\theta = 60°$ (case C).

and film height. Further details on the film boundary condition adopted in this study can be found in Refs. [28, 36]. In cases B and C, the majority of droplets enter the combustion chamber with a lower axial velocity component with respect to case A where almost whole the liquid fuel enters the combustion chamber without filming. Therefore their capability to reach the same axial locations further downstream is reduced as well together with their capability to cross the shear layer from the inner region to the outer region nearby the exit of the injector cup. The effect of such different interactions can be observed quantitatively on the droplet velocities in the combustion chamber. The axial ($U_{p,z}$), radial ($U_{p,r}$) and tangential ($U_{p,\theta}$) velocity profiles of the liquid fuel are presented in Figs. 3I& 3II at two different axial locations, $z = 2.5$ mm and $z = 5$ mm respectively, located as indicated by the two horizontal lines in Fig. 2-(bottom row), for the three different injection angles. Note that droplet velocities are divided in two groups, using a threshold value of droplet diameter $d_p = 10\,\mu$m, to highlight the Stokes number effect and plots are presented as joint-pdf of space and velocity to better visualize the regions where the liquid density is higher. Finally, for a better comparison between the different charts the mean gaseous velocity profile for each component is added as a reference (dashed black lines).

Close to the chamber backplane, Fig. 3I, the two groups of droplets present different dynamics. The ones with small diameters mainly behave as tracers and follow the gaseous velocity profiles independently of the injection angle, Fig. 3I-(left plots). This first observation suggests that the injection condition, as well as the velocity at which they are released at the edge of the injector cone by the liquid film layer, is not sufficient to overcome their tendency to follow the gaseous field. Further proof of this behaviour is the wider variation observed for all of the liquid velocity components for such small droplets, their trajectory does not depend on the injection system or the liquid film layer because small scale turbulent fluctuations are leading. On the contrary, the inertial response prevails for the droplets with larger diameters, Fig. 3I-(right plots). Indeed, when $\theta = 35°$, the liquid axial velocity $U_{p,z}$, Fig. 3IA-(top row), is always higher than the gaseous streamwise component. For this reason a large amount of droplets is found to concentrate on the outer region of the shear layer. On the contrary, when $\theta = 60°$, Fig. 3IC-(top row), the droplet velocity is strongly reduced by the liquid film and the majority of liquid fuel remains locally confined inside the shear layer. Finally, with $\theta = 45°$, Fig. 3IB-(top row), an intermediate result is obtained and both droplets crossing the shear layer and with lower axial momentum are found. Radial and tangential components, Fig. 3I-(middle row) and Fig. 3I-(bottom row), further confirm this tendency.

Looking at the same information at a second location at a larger distance from the chamber backplane, Fig. 3II, the difference in Stokes numbers is seen to have a major impact on the droplet trajectories than the dependency on the injection condition which is here almost negligible if compared to Fig. 3I, when it comes to both droplet spatial distribution and velocity.

Views of the mean spatial distribution of droplet diameters are displayed in Fig. 4 for the three different cases; the black line representing the flame shape (ten percent of maximum heat release rate) and some iso-lines of equivalence ratio are displayed in white. Overall the same droplet spatial distribution is retrieved in the three cases suggesting that the liquid trajectory is mainly driven by the aerodynamics of the gaseous flow even though small differences can be noticed essentially due to the different velocities registered for the liquid phase at the entrance of the combustion chamber. Indeed, fast droplets which are able to cross the high intensity shear regions from the inner to the outer side at the flame root are found to be able to reach the external side of the flame tip before being evaporated, Fig. 4A. In the other two cases the location of the peak corresponding to the presence of large droplets is slightly lower in terms of streamwise position and at a larger radial location. The different droplet dynamics, confirmed by the different spatial distributions of droplet diameters, have a direct impact on the gaseous fuel field. This is highlighted in Fig. 4 by the contour lines of equivalence ratio. The large velocity at which large droplets enter the combustion chamber in case A, results in steep gradients of equivalence ratio in the radial direction (small distance between the white lines). On the contrary, in cases B and C, the sustained presence of the film layer on the injector wall and the associated reduction of the droplet velocity leads to smoother gaseous equivalence ratio radial gradients suggesting a more homogeneous gaseous fuel distribution, Fig. 4B & C.

The resulting flame shapes are compared in more detail against the experimental visualization in Fig. 5 showing fair agreement for the three cases. The flame root positions itself

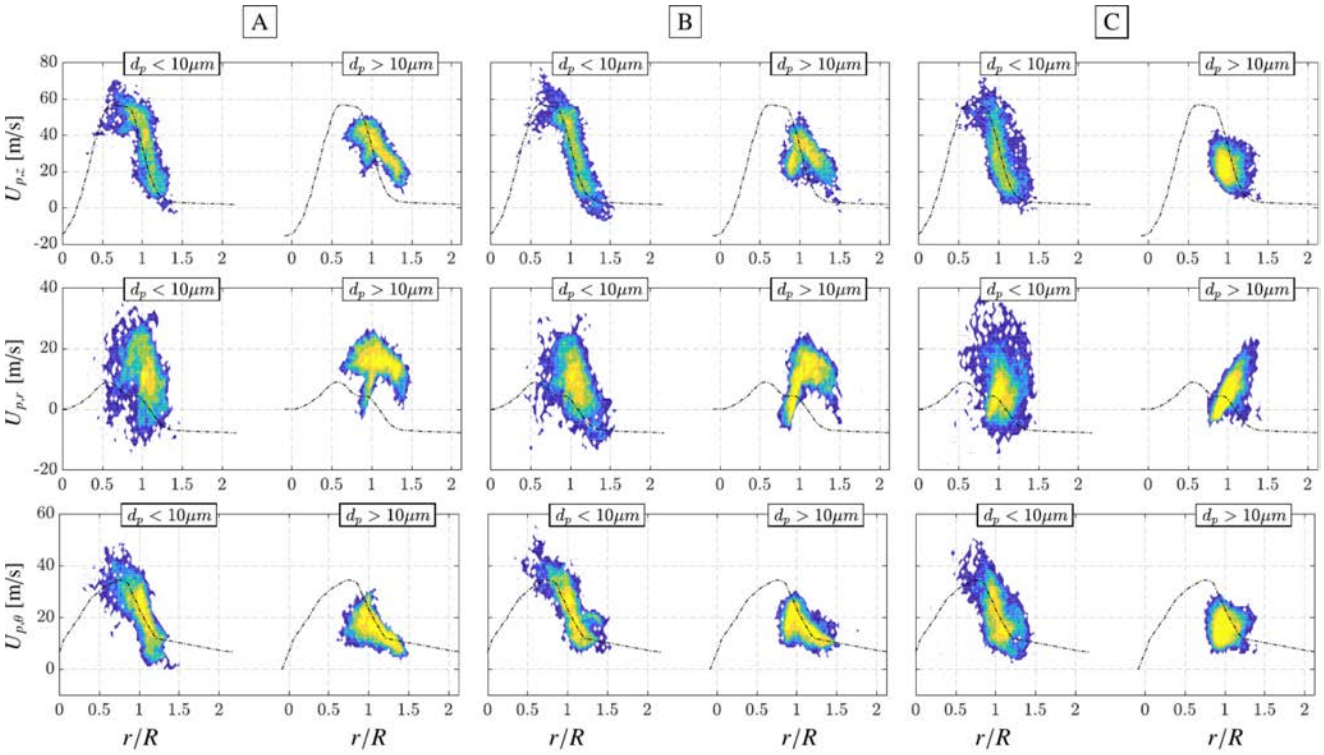

(I) $z = 2.5$ mm

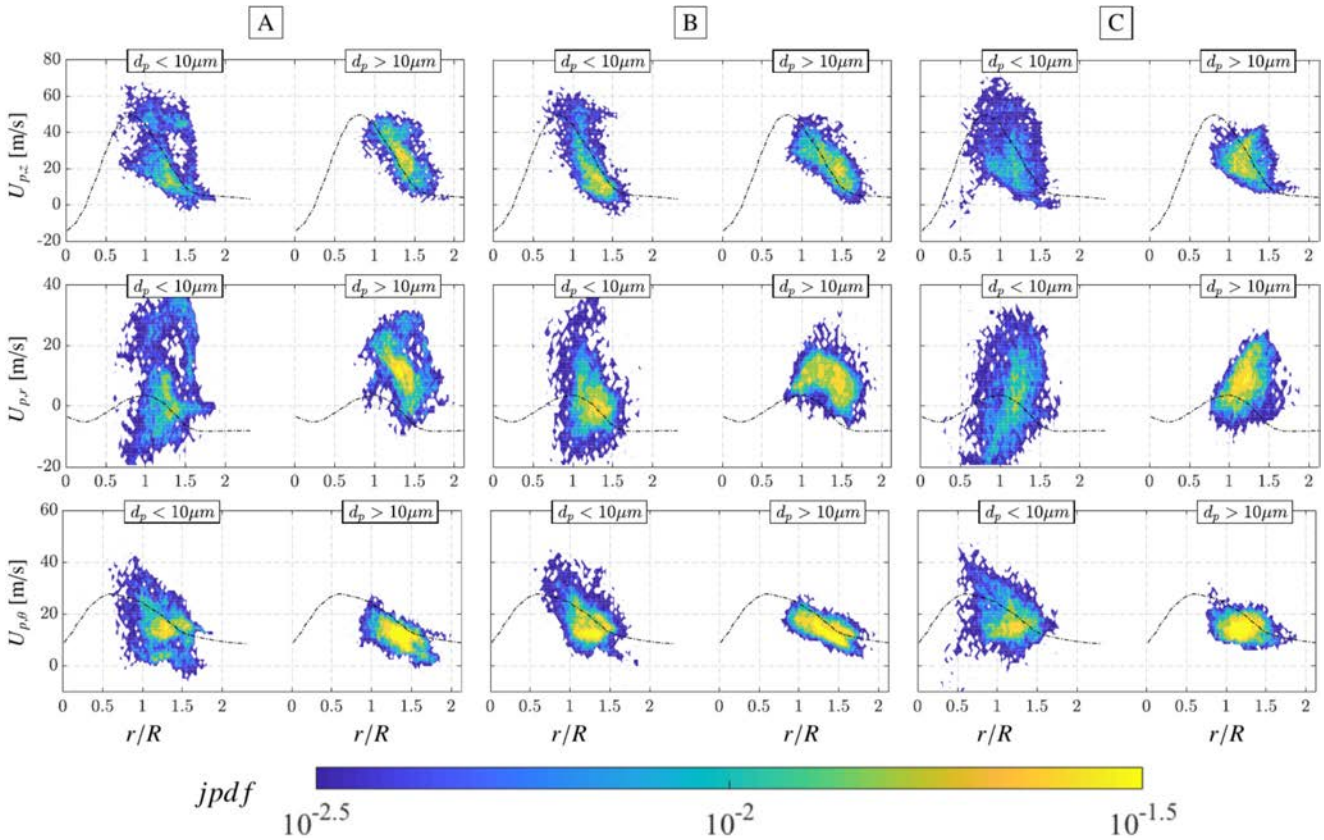

(II) $z = 5$ mm

Figure 3: Liquid velocity spatial distribution in a plane at $z = 2.5$ mm (I) and $z = 5$ mm (II) from the combustion chamber backplane presented as a joint pdf in logarithmic scale. In each subfigure, from top to bottom: axial, radial and tangential velocity; from left to right: injection angles $\theta = 35°$ (case A), $45°$ (case B) and $60°$ (case C). For each chart, two liquid droplets groups characterized by a diameter smaller (larger) than $d_p = 10\,\mu$m are plotted on the left (right) together with the corresponding mean gaseous velocity (black dashed line).

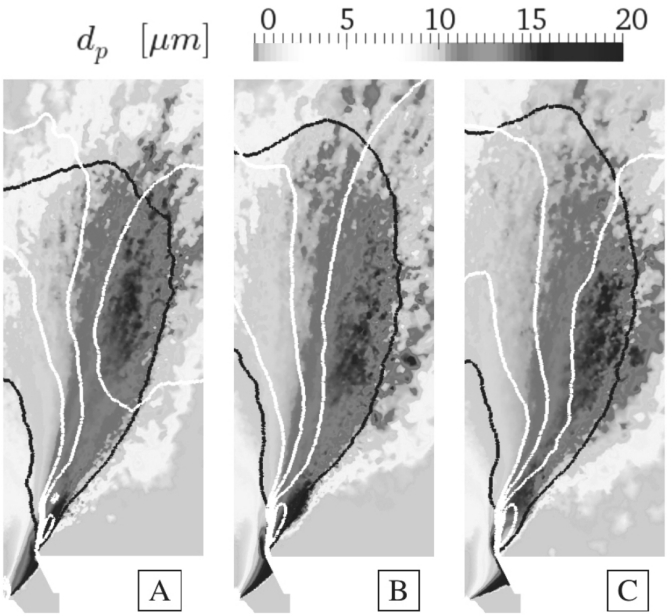

Figure 4: Droplet diameter distribution within the combustor for the three injection angles θ = 35° (case A), 45° (case B) and 60° (case C). Black line indicates contour of $\dot{q}$ = 30 MW/m^3 (10% of maximum heat release rate), white lines indicate equivalence ratio contours at ϕ = 0.65, 0.75, 0.85, 0.95.

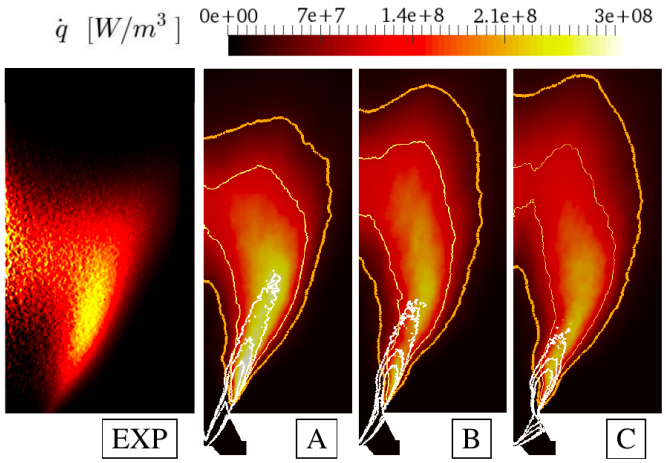

Figure 5: Flame shape comparison: CH* chemiluminescence [25] and mean heat release rate fields from the simulations for the three injection angles θ = 35° (case A), 45° (case B) and 60° (case C). White contours corresponding to mass transfer Γ = 1.5, 5, 20 Kg/m^{3}s, the orange contours corresponding to heat release rate values $\dot{q}$ = 30 MW/m^3 (10% of maximum heat release rate) and $\dot{q}$ = 100 MW/m^3.

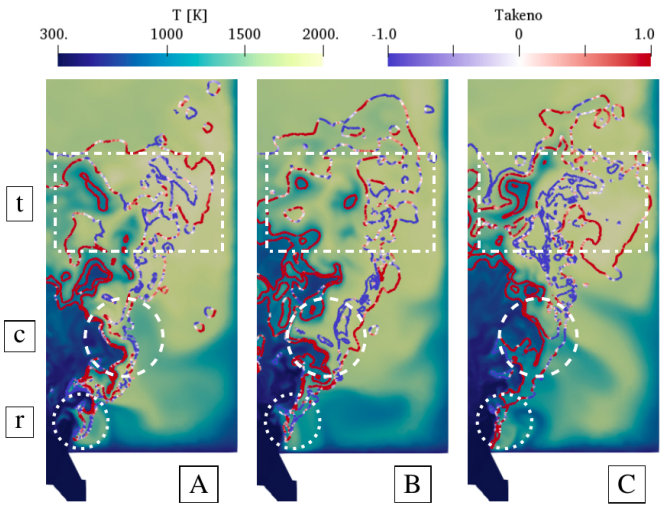

Figure 6: Instantaneous temperature field for the three injection angles θ = 35° (case A), 45° (case B) and 60° (case C). The heat release rate isoline at $\dot{q}$ = 30 MW/m^3 (10% of maximum heat release rate) is used to represent the flame region and it is coloured with the Takeno flame index showing the premixed (red) and diffusion (blue) flame regions. The flame is divided into three different regions representing the flame root (r), center (c) and tip (t).

at similar anchoring points and lift-off heights are equivalent for the three injection angles suggesting that the different liquid dynamics have a minor impact on the flame stabilization process. The mean flame angle also remains the same in the three cases as well as the overall flame location. However, even if the same levels of heat release rate are registered, the most visible effect appears through the total flame surface. Indeed, using the contour at ten percent of maximum heat release rate (bold orange line in Fig. 5), the flame length is seen to increase with the injection angle θ. The shorter flame is balanced in case A by a more intense heat release rate zone in the lower flame region if compared to case C, whereas stronger similarity is visible for cases B and C. The distribution of the evaporation rate displayed by the white contours of fuel mass transfer between liquid and gaseous phase confirms a different penetration of the liquid jet, which is found to decrease with increasing θ, showing also larger distance between each iso-line. As previously deduced, this result further confirms the smoother gradients of gaseous equivalence ratio in Fig. 4: increasing the injection angle results in a more uniform distribution of fuel concentration due to an increased localization of the evaporation rate near the flame root.

In Fig. 6, instantaneous temperature fields and flame contours coloured by the Takeno flame index highlight the complexity of the present flames which are characterized by both premix and diffusion combustion regimes, a common feature in spray flames [28, 33, 37]. To better investigate the effect of the different injection angles on the flame structure, a local analysis is performed for three flame regions as shown in Fig. 6: flame root (r), flame center (c) and flame tip (t). This analysis is displayed in Fig. 7 where the scatter plot of temperature is plotted as a function of the local mixture fraction. Premix and diffusion flame regimes are displayed for each case and the transparency indicates the occurrences of the specific state. In each plot, the gray dash-dot vertical line indicates stoichiometric mixture and the black dashed vertical line refers to the mixture fraction corresponding to the global equivalence ratio (ϕ_{gas} = 0.85). Scatter plots are superimposed to three laminar gaseous counterflow flame curves obtained at different strain rates (a_T): $a_T \simeq$ 150, 250 and 340 s^{-1} [38].

At the flame root, Fig. 7-(top row), common features can be observed regardless of the spray injection angle: the diffusion combustion regime prevails confirming that the flame in this zone is mainly driven by droplet evaporation. Released fuel va-

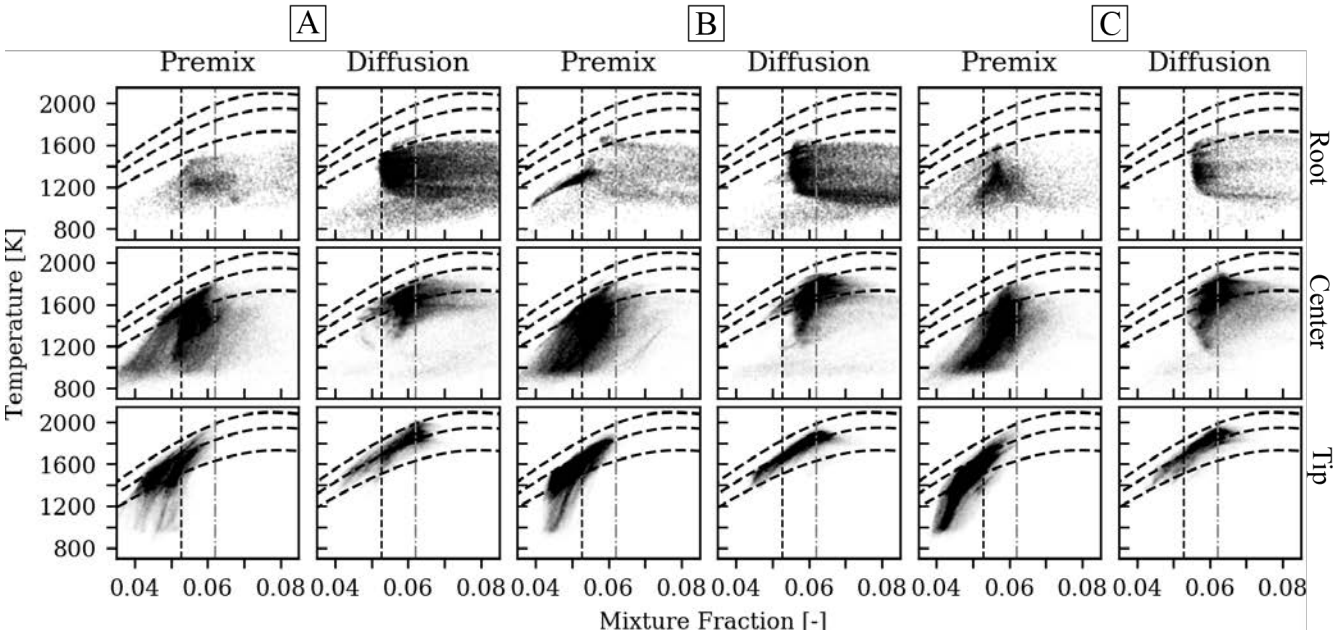

Figure 7: Scatter plot of the flame structure in the plane temperature-mixture fraction. The flame regions are highlighted in Fig. 6, the same analysis is presented for the three different injection angles, $\theta = 35°$ (case A), 45° (case B) and 60° (case C). The two combustion regimes, premix and diffusion, are plotted on different charts. The gray dash-dot vertical line indicates stoichiometric mixture while the black dashed vertical line refers to the mixture fraction corresponding to the global equivalence ratio ($\phi_{gas} = 0.85$). Other dashed lines correspond to laminar counterflow flames at increasing strain rate $a_T \simeq 150$, 250 and 340 s^{-1}.

por is immediately burned with the surrounding oxygen mainly at stoichiometry, but, as often observed in evaporation driven flames [33], a broadening of the scatter in the rich side is observed due to the strong evaporation happening in this region. The previously discussed effects resulting from the different injection angles on the droplet dynamics are here visible through the combustion regimes at the flame root. When injecting at $\theta = 35°$ the premixed flame is almost negligible. Increasing the injection angle instead, cases B and C, the rich side of the diffusion flame reduces in favour of a larger region characterized by premixed combustion. This result may be linked to the different droplet momentum in this region. In case A, where the droplets cross the flame front thanks to their higher axial velocity, it is locally not possible to have a complete fuel-air mixing and the flame burns in an evaporation driven regime where fuel is consumed as soon as it becomes gaseous. For the other two cases, premix regime is favored by the reduced velocity induced by the strong interaction with the injector cup, as it is confirmed by the previously observed higher concentration of liquid mass transfer at the flame root when increasing the injection angle (white lines in Fig. 5).

In the flame central region, Fig. 7-(middle row), premixed combustion is more pronounced and rich combustion spots almost disappear. Flame structures for cases B and C are again very similar whereas the premixed flame region appears less pronounced in case A, due to the flame root behaviour. However, and in agreement with the reported droplet dynamics, the impact of the injection angle weakens when going further downstream. The premixed region is constrained between the stoichiometry and local equivalence ratios lower than the global value. At stoichiometry, the flames feature a maximum temperature $T = 1900$ K and are almost superimposed to the $a_T \simeq 250$ s^{-1} counterflow flame curve. In the leaner regions, they detach from this curve reaching very low temperature. These spots are positioned on the inner side of the jet where the cold air is still penetrating the combustion chamber but the flame is sustained externally thanks to the stoichiometric zones. Indeed, looking at the snapshot of Fig. 6, the structure in this region is most likely diffusive on the external side of the swirled jet and premixed on the internal side. It is worth noticing that the possibility of such lean and cold premixed spots are specific to these two-phase swirled flames where blow off is avoided by the external side flame that is fed by liquid fuel [39].

Finally, the flame tip region is mainly characterized by very lean combustion, Fig. 7-(bottom row). In this specific region, the three flames show very similar behaviours because, at this location, the majority of the fuel is already evaporated and the effect of the liquid fuel dynamics is therefore less significant. Both premixed and diffusion branches follow mainly the counterflow flame curves except for the leaner zone where they detach from these curves moving towards lower temperature regions. Regarding the premixed regime, where this effect is more visible, the reason is again the low temperature spots which may be induced by the central jet of air penetrating the combustion chamber. Note also the diffusion regime which extends on the lean region, contrarily to the flame root, because few droplets reach this zone and burn quite fast in the lean mixture. The two evaporation driven regimes, at the flame tip and flame root, differ in terms of fuel availability which is in excess at the flame root and scarce in this region.

To conclude on the stationary case, overall the mean flame shape is almost not affected by variations of the injection angle. The flame structure and shape, in its general features, are unchanged except for the slight increase of flame length when increasing the injection angle. The detailed analysis of the flame, i.e. looking at the droplet dynamics and flame structure, Figs. 3I & 7-(top row), however suggests that differences arise mainly due to the way the liquid fuel enters the combustion chamber. In that respect, a change in the liquid phase injection angle results in different timescales of the droplets relative to the gaseous timescales present near the exit swirler region. More specifically, on the injector outer lip, where a liquid film can form depending on the injection conditions, will yield different interactions between the two phases in this specific region. Such ratio of timescales does not have a significant impact on the overall statistically steady solution since the local synchronization of phenomena is not a leading mechanism for such conditions. When going to thermoacoustically unstable conditions instead, the resonating mechanism implies a chain of events which needs to be perfectly tuned otherwise the feedback loop between the flame oscillation and the acoustic field is not closed and the limit cycle is not sustained. The second part of this work aims at showing the importance of such a chain of events stressing the influence of the injection angle, and the interactions at the injector wall.

3.2. Self-excited limit cycle

The self-excited condition is searched with LES, starting from the previous simulations but increasing the flame tube length to $\ell_c^{(2)} = 280$ mm. Figure 8 shows the temporal evolution of the pressure signal at the chamber backplane for the configuration with an injection angle $\theta = 45°$. Starting from the previously discussed stable flame (Fig. 5B), a linear amplification of the oscillations appears followed by an exponential amplitude growth leading to an overshoot and finally to a saturation yielding a stable limit cycle of amplitude $p'_{LES} \simeq 2000$ Pa at a sustained oscillation frequency $f_{LES} \simeq 500$ Hz. These results are in line with the experimental measurements ($p'_{exp} \simeq 1700$ Pa and $f_{exp} \simeq 530$ Hz [27]), as extensively discussed in the previous publication of the same authors [28]. Given the marginal impact of the injection angle on the stable solution, the limit cycle computations for cases A ($\theta = 35°$) and C ($\theta = 60°$) are initialized using the reference case B but starting at $t_\theta = 110$ ms, as indicated in Fig. 8. Doing so, the linear growth and the overshoot regions for cases A and C are avoided reducing the overall CPU cost of these simulations. Figure 9 shows the time traces of the pressure fluctuations and heat release rate for the three different injection angles started after t_θ. Clearly, when switching to $\theta = 35°$ (case A), the system is not able to hold the oscillation for a long time. On the contrary, synchronization between pressure and heat release rate fluctuations remains when the spray angle is increased. The oscillation frequency in the two unstable cases (cases B & C) is the same although a slightly lower amplitude is reached with case C. In terms of flame shape, during the limit cycle oscillation, the experimental observation and both LES oscillating cases are found in good agreement (Fig. 10). Small differences are visible between the two simulations during the positive pressure fluctuation (p'_{max}), at the flame center, where for $\theta = 60°$ a zone of higher heat release rate is observed. This could be a consequence of the different velocity at which droplets enter the combustion chamber in the two cases. As already discussed for the stable flame, the fast droplets not passing through the film layer of case B will evaporate and burn in the outer side of the flame. On the contrary, in case C all the droplets will be released by the film layer. These will then be characterized by a low velocity and will be more prone to follow the dynamics of the gaseous phase that is oscillating following the thermoacoustic limit cycle. As a consequence, a large number of droplets is expected to be trapped by the central recirculation zone resulting in a more intense heat release rate in this region.

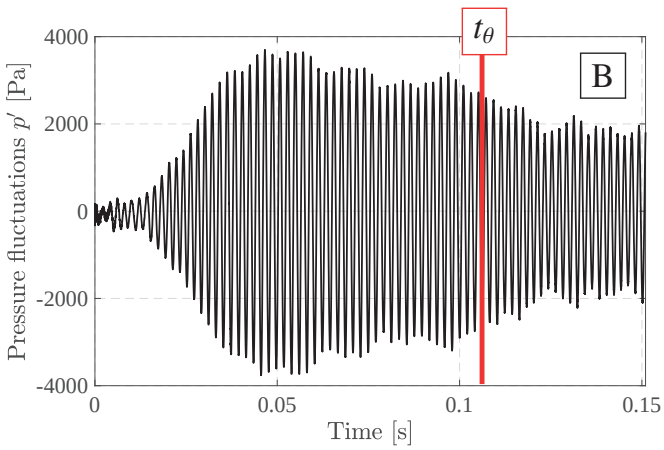

Figure 8: Pressure signal at the chamber backplane obtained for the limit cycle when $\theta = 45°$ (case B). Figure reproduced from Ref. [28].

3.2.1. Film layer dynamics

To better understand the reasons leading to the system stabilization for case A and sustained oscillations for cases B & C, Fig. 11 shows instantaneous contours of liquid volume fraction α_ℓ for both cases A & C at three specific instants of the early limit cycle starting at t_θ. With such a view it is confirmed, accordingly with Figs. 4 & 5, that the main driver appears to be the liquid film, which for case A is rapidly washed away as time proceeds whereas for case C it remains and responses to the external acoustic modulation. As detailed hereafter, cases B & C, produce similar observations although the response of the film layer differs slightly explaining the limit-cycle differences. Focusing on this aspect, Fig. 12 shows the non-dimensional film height fluctuations $h'/\overline{h}$ along each film local coordinate ξ, with origin positioned at the lower edge of the injector cone. First, one notes that, as expected, a different injection angle implies different impact points on the outer injector wall (respectively noted by $\xi_I^B \approx 2.2$ mm and $\xi_I^C \approx 1$ mm) which results in different film extents: $\xi \in [1.3, 5.6]$ mm for case B and $\xi \in [0, 5.6]$ mm for case C. Then, comparing the two temporal evolutions of the film height fluctuation, it is possible to observe that the film region responding to acoustics is also different in the two cases. In case B, large variations of

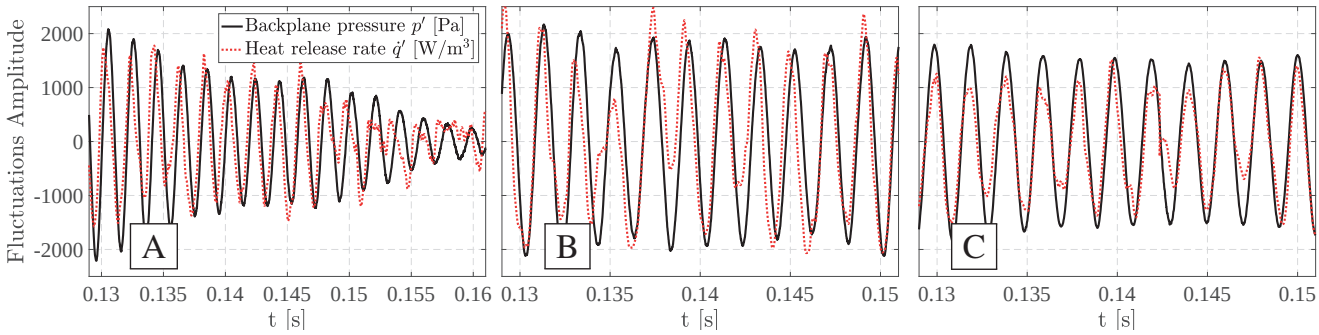

Figure 9: Pressure fluctuations at chamber backplane and heat release rate oscillation for the three different injection angles $\theta = 35°$ (case A), 45° (case B) and 60° (case C). Oscillation frequencies obtained via FFT of the pressure signal: $f_A = 495$ Hz, $f_B = 492$ Hz and $f_C = 498$ Hz.

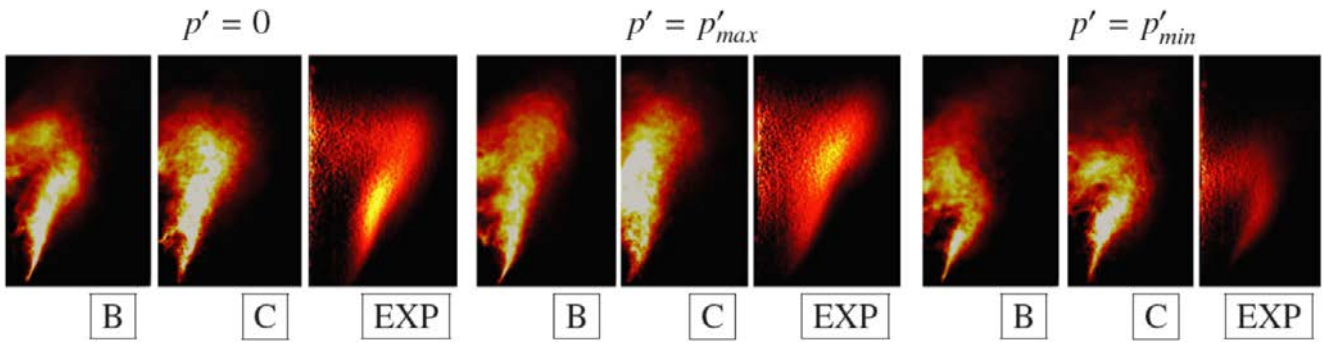

Figure 10: Heat release rate phase average over ten limit cycles obtained with $\theta = 45°$ (case B) and 60° (case C) compared to experimental CH* chemiluminescence [25].

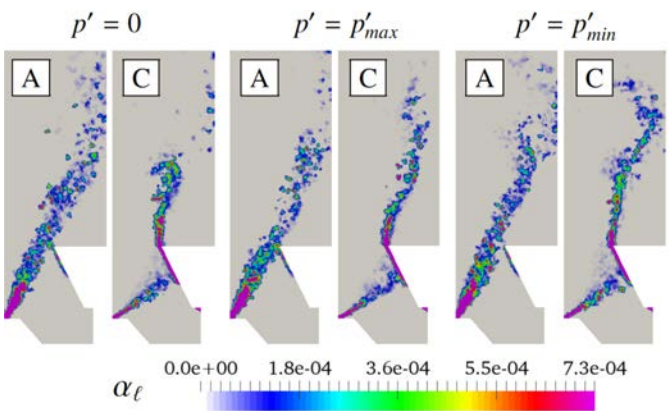

Figure 11: Liquid volume fraction α_ℓ for injection angles $\theta = 35°$ (case A) and 60° (case C).

h' are obtained only in the second half of the liquid sheet, i.e. for $\xi \in [3.5, 5.6]$ mm, where for case C the oscillations instead occur over a larger area ($\xi \in [1.3, 5.6]$ mm). Note that the location at which the oscillations start seems linked to the point at which the hollow cone jet impacts the injector wall (ξ_I^B and ξ_I^C), these two coordinates could be then considered as a node of the film thickness fluctuation. Starting from these points, differences appear: in case B, at the positive pressure fluctuation anti-node (red circles curve), it is possible to note that all points of the film fluctuate with the same phase and with an amplitude that increases almost monotonically with ξ until reaching the droplet release point. On the contrary, in case C, the film layer shows spatial variations of phase, i.e. $\xi \in [2, 4]$ mm and near the film edge $\xi \in [4.5, 5.6]$ mm. At pressure fluctuation peak within the cycle (red curve with circles in Fig. 12), a maximum of fluctuation amplitude in the central film region corresponds to almost no height variation at the edge of the injector where droplets are released and vice-versa for the pressure node (blue curve with triangles in Fig. 12).

Different film dynamics necessarily imply different fuel variations at the flame root, since the release of droplets at the edge of the injector wall is driven by the liquid film. To better understand the coupling between the film and acoustics, a film oscillation frequency f_f can be introduced for the liquid layer as the ratio between the film mean characteristic velocity U_f and its extension length that is oscillating L_f^{osc} (evaluated from Fig. 12). Note also that, since the adopted film modeling assumes a droplet film velocity that is directly proportional to its local thickness (h_0) and local wall shear stress($\tau_{w,0}$): $U_{f,0} \sim \tau_{w,0} h_0 \mu_0$ (more details in Ref. [36]), one can easily evaluate a film velocity. In case B, the simulations give an average film thickness $H_f^B \simeq 8\,\mu$m which results in a mean velocity of $U_f^B \simeq 1.3$ m/s oscillating with a characteristic film frequency, $f_f^B = U_f^B / L_f^{osc,B} = 1.3/0.0025 = 520$ Hz. In that case, the film dynamics is found to be in full synchronization with the thermoacoustic eigenmode. For case C, the film is thicker, $H_f^C \simeq 12\,\mu$m resulting in a faster mean film velocity, $U_f^C \simeq 2.8$ m/s. This seems to be expected since when $\theta = 60°$, almost all the

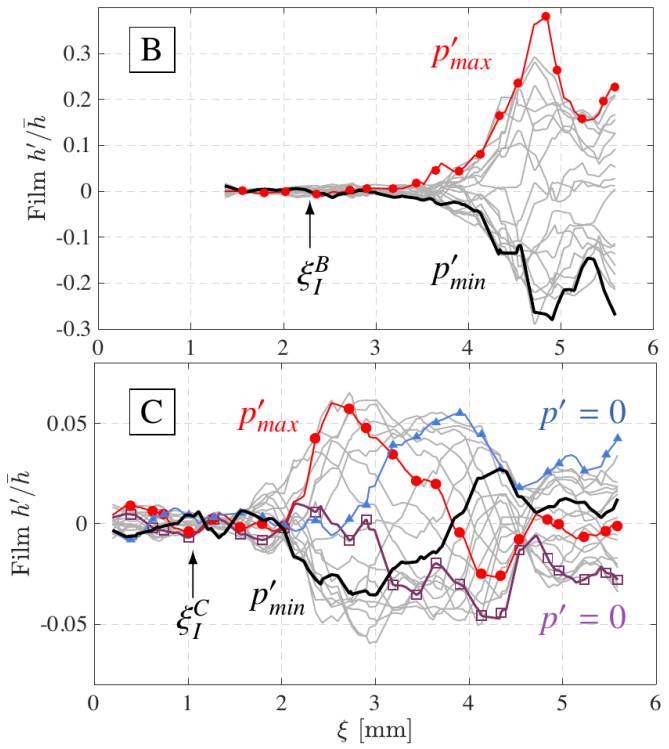

Figure 12: Acoustic response of the liquid film layer for $\theta = 45°$ (case B) and 60° (case C). The plot for case B is reproduced from Ref. [28]. The coordinate ξ is rescaled positioning the origin at the bottom edge of the injector cone.

injected fuel impinges the injector wall contrarily to the other two cases. The film dynamics is thus characterized by a higher characteristic frequency: $f_f^C = U_f^C / L_f^{osc,C} = 2.8/0.0043 = 650\,\text{Hz}$ which does not perfectly tune with the acoustics eigenmode anymore. Indeed, for this latter case, a phase shift between the two oscillating processes can easily be computed as $\Delta\varphi = (1/f_{LES} - 1/f_f^C)\,2\pi f_{LES} = 83°$ which is very close to 90°, i.e., the limit value required to have a constructive coupling between the oscillation of liquid and gaseous phases at the flame root. Indeed, the system being unstable in cases B & C, the global Rayleigh criterion is satisfied for both computations as shown already in Fig. 9.

3.2.2. *Spray, flame and acoustics correlation indices*

In the following, the LES data are post-processed using Dynamic Mode Decomposition (DMD) [40] algorithm to reconstruct the oscillating modes of the system and to study the system response at a given frequency. For the present simulations the mode of interest, to be retrieved with DMD, is at the limit-cycle frequency and corresponds to the spatial trace of the thermoacoustic system response. To capture this mode the DMD algorithm takes as an input the full set of 3D fields, counting around 200 snapshots, and uses the whole set of variables of interest for both the gaseous and liquid phases: i.e. pressure, velocity, heat release rate, mass transfer rate and liquid volume fraction. Using the resulting modes at the limit cycle frequency, it is possible to investigate the spatial features of each variable oscillation setting its phase with respect to a reference signal,

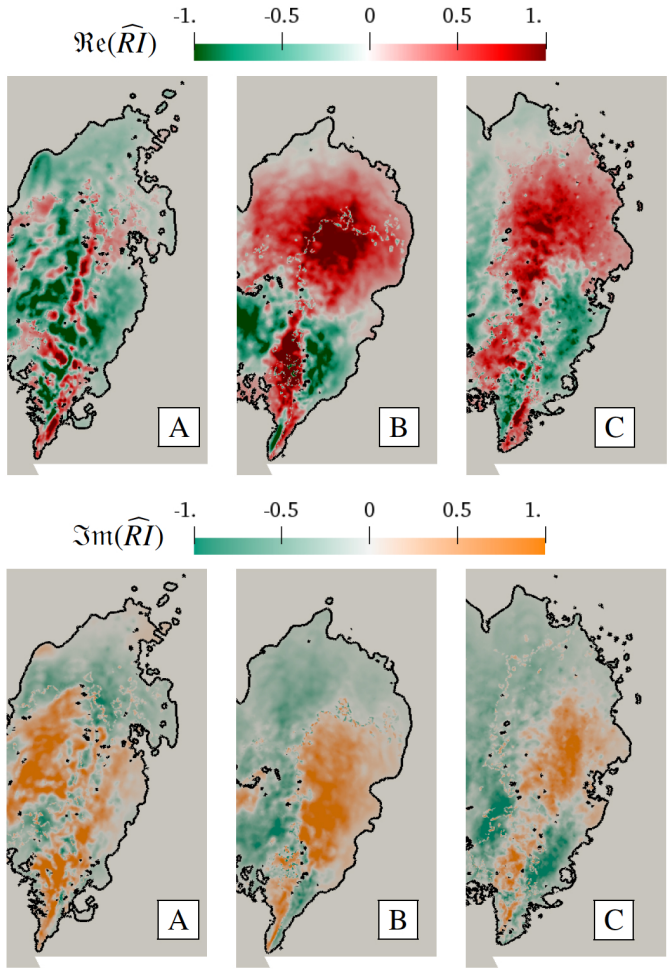

Figure 13: Normalized real and imaginary part of the Rayleigh index formulation in frequency domain, $\Re\mathrm{e}(\widehat{RI})$ and $\Im\mathrm{m}(\widehat{RI})$ in top and bottom row, respectively, for the three injection angles $\theta = 35°$ (case A), 45° (case B) and 60° (case C). The black contour refers to $|\hat{q}| = 30\,\text{MW/m}^3$.

which is here pressure [41]. Doing so, a vision of the Rayleigh index spatial distribution is made available: i.e. the phase lag between the heat release and pressure fluctuations.

As recently pointed out by Magri *et al.* [42], writing the energy balance in the frequency domain allows a more general formulation of the Rayleigh index, $\widehat{RI}$, which is helpful to individuate regions contributing to the enhancement or damping of the instability through its real part $\Re\mathrm{e}(\widehat{RI}) = \mathcal{T}_{q,p} = |\hat{p}|\,|\hat{q}|\,\cos(\varphi_q - \varphi_p)$, where $\hat{\cdot}$ indicates complex quantities. This index, normalized for a convenient reading is shown in Fig. 13-(top row) for the three simulations where it is conditioned on the flame region shown by the black line (taken at $|\hat{q}| = 30\,\text{MW/m}^3$). Looking at the map of $\Re\mathrm{e}(\widehat{RI})$ for case A, for which the pressure oscillation is damped, the system shows large regions of negative contributions as well as less coherent regions of positive values. Contrarily, for conditions B & C, the overall distribution is more likely destabilizing and, since the flame shapes are alike during the limit cycle (Fig. 10), the flame contributions are also similar to the exception of highly local small differences. At the flame root of case B, a highly positive contribution appears together with a small negative re-

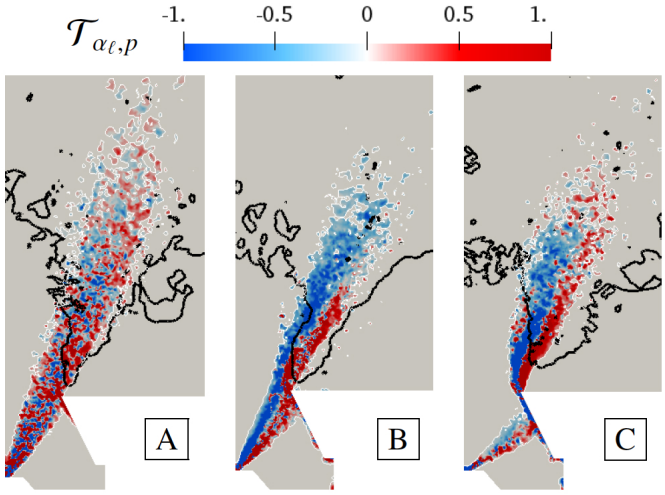

Figure 14: Normalized liquid fuel-pressure fluctuations correlation index $\mathcal{T}_{\alpha_\ell,p}$ for the three cases $\theta = 35°$ (case A), 45° (case B) and 60° (case C). Black contour refers to $|\hat{q}| = 30\,\mathrm{MW/m^3}$.

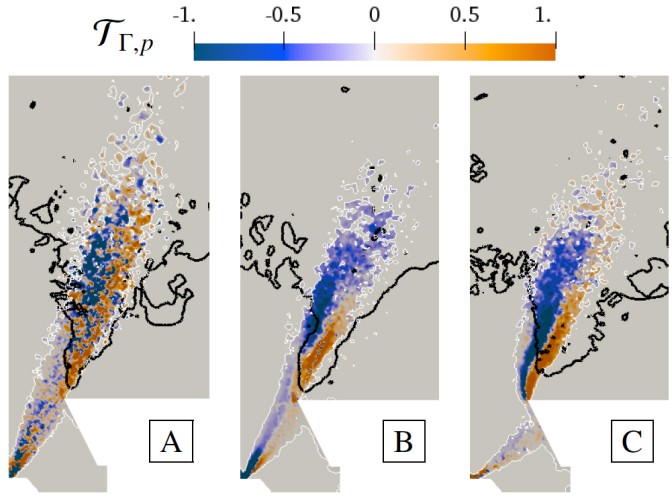

Figure 15: Normalized evaporation-pressure fluctuations correlation index $\mathcal{T}_{\Gamma,p}$ for the three cases $\theta = 35°$ (case A), 45° (case B) and 60° (case C). Black contour refers to $|\hat{q}| = 30\,\mathrm{MW/m^3}$.

gion. For case C, lower $\Re\mathrm{e}(\widehat{RI})$ amplitudes of both signs appear broadened in the radial direction. Moving further downstream, the main flame of case B presents a large positive area of $\Re\mathrm{e}(\widehat{RI})$ spanning the entire top part of the flame. Intense damping is located in the residual swirl shear layer region as well as within the recirculation zone. In case C these negative contributions locate similarly but spanning a larger area with a lower intensity. Figure 13-(bottom row) displays the normalized spatial contributions to the imaginary part of the complex Rayleigh index, $\Im\mathrm{m}(\widehat{RI}) = |\hat{p}|\,|\hat{q}|\,\sin(\varphi_q - \varphi_p)$, which, as pointed out by Magri *et al.* [42], can be analyzed to further study the local effects in terms of variation of the resonant frequency due to the thermoacoustic coupling [43]: the regions presenting heat release rate and pressure fluctuations in quadrature (maxima and minima of the colormap in Fig. 13-(bottom row)) are the one maximising the frequency of the limit cycle. With respect to its real counterpart (Fig. 13-(top-row)), the spatial distribution of $\Im\mathrm{m}(\widehat{RI})$ shows a higher coherence between the stable and unstable cases, a result that is in line with what is shown in Fig. 9 where, also for the stable case A, pressure and heat release rate oscillate at the same frequency regardless of the imposed spray angle.

The complexity of the present liquid fueled system thermoacoustic response can be better understood looking at the coupling between the spray and acoustics. Using DMD of the liquid volume fraction α_ℓ similarly to the Rayleigh Index, a liquid fuel-pressure fluctuation correlation index $\mathcal{T}_{\alpha_\ell,p}$ can be introduced,

$$\mathcal{T}_{\alpha_\ell,p} = |\hat{\alpha}_\ell|\,|\hat{p}|\,cos(\varphi_{\alpha_\ell} - \varphi_p). \tag{1}$$

Figure 14 displays the normalized spatial distribution of $\mathcal{T}_{\alpha_\ell,p}$ obtained with the three different injection angles. For the stable case A, $\mathcal{T}_{\alpha_\ell,p}$ does not reveal any coherent field suggesting that, when injected at $\theta = 35°$, the liquid fuel enters the combustion chamber without being synchronized with the limit cycle frequency. On the contrary, for the two cases featuring a limit cycle, a clear shape appears with local differences that can be linked to the differences present in the region of the injector wall. Indeed, in case B, the liquid released by the film oscillation results in a positive contribution to the instability right after the edge of the injector as a consequence of phase coupling between the film thickness oscillations and pressure previously discussed (Fig. 12B). On the contrary, the droplets entering the combustion chamber straight from the injection point are responsible for the negative values of $\Re\mathrm{e}(\widehat{RI})$, since their phase relative to the pressure signal is not affected by the liquid film layer. In case C, all injected droplets pass through the film layer which, in this case, is not perfectly tuned with the limit cycle (Fig. 12C). The positive coupling between pressure and heat release is therefore achieved further downstream the injector exit, as shown by the $\Re\mathrm{e}(\widehat{RI})$ map of Fig. 13C-(top row), with the participation of a flapping oscillation visible in Fig. 14C induced by a variable release of fuel at the edge of the injector.

Focusing on the liquid fuel evaporation rate and pressure fluctuations, similarly to the previously defined $\mathcal{T}_{\alpha_\ell,p}$, an evaporation rate-pressure fluctuation correlation index can be defined as,

$$\mathcal{T}_{\Gamma,p} = |\hat{\Gamma}|\,|\hat{p}|\,cos(\varphi_\Gamma - \varphi_p), \tag{2}$$

where Γ is the mass transfer from the liquid to gas of the evaporating specie. The normalized spatial distribution of $\mathcal{T}_{\Gamma,p}$, computed again using DMD, is displayed in Fig. 15. The resulting map clearly resembles the one obtained for $\mathcal{T}_{\alpha_\ell,p}$, Fig. 14, suggesting that evaporation fluctuations are in phase with the ones of liquid volume fraction. This implies that, even if evaporation is affected by the injection angle in terms of mean field (white lines in Fig. 5), this process is not playing a key role in the flame dynamics which is mainly supported by the local fluctuations of liquid fuel available. This essentially indicates that the liquid fuel instantaneously evaporates and burns without introducing any further delay in the loop as suggested by Vignat *et al.* [24]. Note finally that for cases B & C, the sign of $\mathcal{T}_{\Gamma,p}$ is almost identical to the one of $\mathcal{T}_{\alpha_\ell,p}$ downstream the chamber backplane. When looking at case A instead, the resulting field

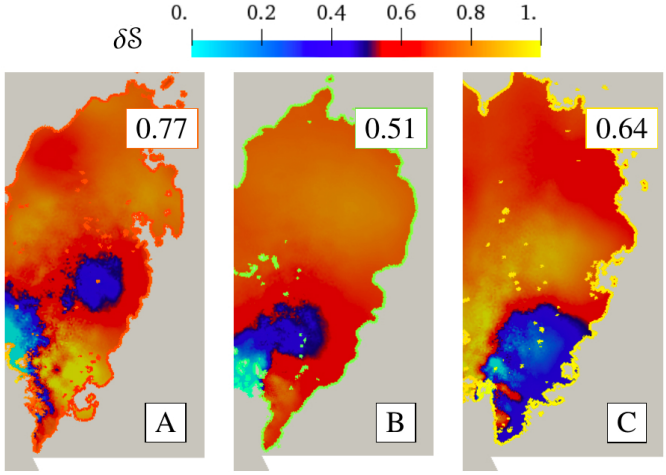

Figure 16: Spatial variations of the sensitivity ($\delta\mathcal{S}$) to the instability for the three cases $\theta = 35°$ (case A), 45° (case B) and 60° (case C). $\delta\mathcal{S} = (\mathcal{S} - \mathcal{S}_{min})/(\mathcal{S}_{max} - \mathcal{S}_{min})$ where $\mathcal{S} \in [0, 1]$. The mean values of sensitivity are computed and displayed in the textbox.

does not present any spatially well organized mode, although the small positive contribution to the instability at the flame anchoring point, Fig. 13A-(top row), is here justified by a slightly more coherent positive region around that point. This specific region is however not sufficient to sustain the instability. Effectively, the spatial distribution of $\mathcal{T}_{\Gamma,p}$ (in terms of amplitude), for all three cases, presents significant contributions that appear only in the combustion chamber, inside the injector the amplitude remaining very small, which confirms that evaporation has a limited effect in this region because of the lower temperature.

3.2.3. System sensitivity analysis using adjoints

To conclude the comparison between the three numerically obtained limit cycles, an evaluation of each simulation stability can be obtained by manipulating the frequency domain expression of the Rayleigh criterion to yield the sensitivity of the pressure fluctuations with respect to heat release rate oscillations [42]. To do so, the adjoint DMD matrix is used to numerically approximate the true Perron-Frobenius operator [44, 45] and computed with the same DMD algorithm applied previously. With this approximation, the resulting eigenmodes are the adjoint DMD modes, noted thereafter p^{+*} for pressure for example. Together with the previous DMD results, it is hence possible to evaluate the sensitivity to heat release variations of each prediction using the simplified formulation $\mathcal{S} = (d\hat{p}/d\hat{q})\hat{q} = \hat{p}^{+*} - (D/C)\hat{p}$ where $C = \int_V \bar{\rho}(\hat{u}^2) + \hat{p}^2/(\gamma\bar{p})dV$ and $D = (\gamma - 1)/(\gamma\bar{p})$ [42]. The maps of the normalized sensitivity variation of each case are shown in Fig. 16 together with their corresponding mean integrated values (textboxes). Starting with the mean sensitivity, provided values are in line with observed limit cycles obtained from LES. In case B, where the oscillation is the strongest because of the pressure and heat release rate synchronization, the overall pressure sensitivity to heat release rate fluctuations is the lowest. On the contrary, a larger value is achieved for the stable condition, case A. This indicates that for $\theta = 35°$ the 500 Hz pressure mode, which is not amplified in this case, is however more sensitive to variations of heat release rate: a condition that may eventually lead to an unstable (more stable) solution, if the spray angle is increased (or further reduced). Equivalently, case C has an increased sensitivity compared to case B which indicates that this case can either become stable or more unstable, again pointing to the potential importance of the liquid film properties in determining the stability of the present burner.

The spatial variations of sensitivity further confirm these conclusions suggesting a link between the flame response and the effect of the injection process. Indeed, except for the upper part of the flame which is contributing to the sensitivity of the instability, it is noticed that in the stable case, Fig. 16A, a higher variability of sensitivity appears at the flame root where the liquid fuel is, in this case, not responding in phase with the limit cycle. Modifying the injection process would therefore be able to change the heat release rate fluctuations in that region implying a significant variation of the system limit cycle mode, eventually resulting in a new unstable solution. When going to the perfectly tuned prediction, Fig. 16B, the spatial distribution of sensitivity looks similar to case A but it also appears more homogeneous. Since the synchronization at the flame root is perfect, it is not easy to move the solution away from the obtained limit cycle, both in the direction of a more unstable solution as well as a stabilized one. Contrarily, when $\theta = 60°$, Fig. 16C, significant changes of this system stability could be obtained if operating on the flame portion located on the central axis of the swirled flow. Note that for this simulation, this specific region coincides with large variations of fuel fluctuations which are believed to contribute to the instability. In other words the obtained limit cycle appears to be more sensitive if compared to case B. As previously discussed, for case C the overall sensitivity of the system is in between the other two solutions but its spatial trend is opposite. Because at the flame root, all the fuel already oscillates in phase with pressure after being entirely released by the film layer, and the lowest sensitivity is found in this region.

4. Conclusions

Spray flames remain a numerical and modeling challenge especially if thermoaoustic instabilities are to be predicted. Although injection parameters are commonly assumed or addressed through various modeling techniques, uncertainties are clearly present. In the case of the Large Eddy Simulations of the SICCA-spray swirled flame, it is shown that an Euler-Lagrange modeling approach is able to produce reasonable results as long as a film modeling is introduced. However, it is also demonstrated here that particular attention is needed when specifying the injection spray angle whose value can be highly affected by the system operating conditions. The proposed discussion indeed specifically focuses on a numerical sensitivity study about the impact of the spray opening value on the SICCA-spray burner. To do so, three cases, $\theta = 35°$, 45° and 60°, are simulated and specific attention is focused on the resulting flame structures and thermoacoustic oscillations. The increase of the angle at which the liquid fuel is injected is found to have only a

minor impact on the stable flame shape whereas it has a major impact on the flame root structures. With $\theta = 35°$, if compared to the other two cases, a different release of fuel by the liquid film layer forming on the injector wall gives rise to different droplet velocities and size distributions in the combustion chamber, in particular at the flame root, which are found to burn in a diffusion flame regime which is predominant if compared to the level of premixedness reached for higher angles.

Contrarily to the stable case, a major impact is observed for the thermoacoustically unstable condition where, depending on the imposed injection angle value, different flame dynamics are retrieved. Contrarily to the experiments, a stable condition is obtained for $\theta = 35°$, i.e., the interaction between the liquid fuel and the injector wall is not sufficient to create a well-established film layer able to couple with the system acoustics. Instead, using $\theta = 45°$ a well-established limit cycle is experienced and a perfect synchronization between the liquid film and the acoustics is observed. A further increase of the injection angle to $\theta = 60°$ still leads to a film-acoustics coupling sufficient to sustain the oscillations but not with a perfect synchronization as in the previous case. Indeed, the phase at which the liquid fuel enters the combustion chamber is shown to be crucial and it is impacted by the film response. To illustrate this finding a liquid fuel-pressure fluctuation correlation index $\mathcal{T}_{\alpha_\ell,p}$ is introduced. The spatial fields of such a variable confirm the synchronization between the liquid volume fraction distribution and the pressure fluctuations when a limit cycle is observed. Similarly, an evaporation-pressure fluctuation correlation index, noted $\mathcal{T}_{\Gamma,p}$, reveals that fluctuations of evaporation play a secondary role if compared to the hydrodynamics fluctuations which drive the presence of the liquid fuel available at the flame root for the oscillation to be sustained. Finally, the overall stability of the present complex simulations is confirmed by investigating the spatial distribution of the Rayleigh criterion formulated in the frequency domain.

To conclude, the spray injection angle is shown for the SICCA-spray burner to be a key parameter that controls the thermoacoustic coupling of this setup even if it has a small impact on the mean flame in non-oscillating conditions. The modifications imposed to the injected fuel are indeed shown to potentially stabilize the system opening new possibilities and strategies for the control of unwanted instabilities.

Acknowledgments

This project has received funding from the European H2020 MSCA-ITN Grant Agreement No 765998 (ANNULIGhT), the ANR16-CE22-0013 (FASMIC) and the MSCA Grant Agreement No 843958 (CLEANERFLAMES - D.L. Individual Fellowship). HPC resources from GENCI (Grant 2020-A0072B10157) and PRACE (Grant CLEANERFLAMES 2019215145) are also acknowledged.

References

[1] S. Candel, Combustion dynamics and control: Progress and challenges, Proc. Combust. Inst. 29 (1) (2002) 1–28.

[2] A. P. Dowling, S. R. Stow, Acoustic analysis of gas turbine combustors, J. Propul. Power 19 (5) (2003) 751–764.

[3] M. Bauerheim, F. Nicoud, T. Poinsot, Progress in analytical methods to predict and control azimuthal combustion instability modes in annular chambers, Phys. Fluids 28 (2) (2016) 021303.

[4] G. Staffelbach, L. Gicquel, G. Boudier, T. Poinsot, Large eddy simulation of self excited azimuthal modes in annular combustors, Proc. Combust. Inst. 32 (2) (2009) 2909–2916.

[5] D. Noh, E. Karlis, S. Navarro-Martinez, Y. Hardalupas, A. Taylor, D. Fredrich, W. Jones, Azimuthally-driven subharmonic thermoacoustic instabilities in a swirl-stabilised combustor, Proc. Combust. Inst. 37 (4) (2019) 5333–5341.

[6] T. Poinsot, Prediction and control of combustion instabilities in real engines, Proc. Combust. Inst. 36 (1) (2017) 1–28.

[7] M. Boileau, S. Pascaud, E. Riber, B. Cuenot, L. Y. M. Gicquel, T. Poinsot, M. Cazalens, Investigation of two-fluid methods for Large Eddy Simulation of spray combustion in Gas Turbines, Flow Turb. Combust. 80 (3) (2008) 291–321.

[8] A. Gosman, E. Loannides, Aspects of computer simulation of liquid-fueled combustors, J. Energy 7 (6) (1983) 482–490.

[9] A. Ghani, T. Poinsot, L. Gicquel, G. Staffelbach, LES of longitudinal and transverse self-excited combustion instabilities in a bluff-body stabilized turbulent premixed flame, Combust. Flame 162 (11) (2015) 4075–4083.

[10] S. Tachibana, K. Saito, T. Yamamoto, M. Makida, T. Kitano, R. Kurose, Experimental and numerical investigation of thermo-acoustic instability in a liquid-fuel aero-engine combustor at elevated pressure: Validity of large-eddy simulation of spray combustion, Combust. Flame 162 (6) (2015) 2621–2637.

[11] T. Kitano, K. Kaneko, R. Kurose, S. Komori, Large-eddy simulations of gas- and liquid-fueled combustion instabilities in back-step flows, Combust. Flame 170 (2016) 63–78.

[12] J. M. Apeloig, F.-X. d'Herbigny, F. Simon, P. Gajan, M. Orain, S. Roux, Liquid-fuel behavior in an aeronautical injector submitted to thermoacoustic instabilities, J. Prop. Power 31 (1) (2015) 309–319.

[13] A. L. Pillai, J. Nagao, R. Awane, R. Kurose, Influences of liquid fuel atomization and flow rate fluctuations on spray combustion instabilities in a backward-facing step combustor, Combust. Flame 220 (2020) 337–356.

[14] F. Giuliani, P. Gajan, O. Diers, M. Ledoux, Influence of pulsed entries on a spray generated by an air-blast injection device: An experimental analysis on combustion instability processes in aeroengines, Proc. Combust. Inst. 29 (1) (2002) 91–98.

[15] T. Yi, D. A. Santavicca, Forced Flame Response of Turbulent Liquid-Fueled Lean-Direct-Injection Combustion to Fuel Modulations, J. Propuls. Power 25 (6) (2009) 1259–1271.

[16] T. Fang, R. E. Coverdill, C.-f. F. Lee, R. A. White, Effects of injection angles on combustion processes using multiple injection strategies in an HSDI diesel engine, Fuel 87 (15) (2008) 3232–3239.

[17] X. Wang, O. A. Kuti, W. Zhang, K. Nishida, Z. Huang, Effect of Injection Pressure on Flame and Soot Characteristics of the Biodiesel Fuel Spray, Combust. Sci. Technol. 182 (10) (2010) 1369–1390.

[18] A. H. Lefebvre, Atomization and Spray, CRC Press, 1989.

[19] J. Ballester, C. Dopazo, Discharge coefficient and spray angle measurements for small pressure-swirl nozzles, At. Sprays 4 (3) (1994) 351–367.

[20] M. Sanjosé, J. M. Senoner, F. Jaegle, B. Cuenot, S. Moreau, T. Poinsot, Fuel injection model for Euler-Euler and Euler-Lagrange large-eddy simulations of an evaporating spray inside an aeronautical combustor, Int. J. Multiph. Flow 37 (5) (2011) 514–529.

[21] S. Chen, A. Lefebvre, J. Rollbuhler, Factors influencing the effective spray cone angle of pressure-swirl atomizers, J. Eng. Gas Turbines Power 114 (1) (1992) 97–103.

[22] E. J. Hopfinger, J. C. Lasheras, Explosive breakup of a liquid jet by a swirling coaxial gas jet, Phys. Fluids 8 (7) (1996) 1696–1698.

[23] M. Govindaraj, K. D. Ghate, M. S. Rao, V. S. Iyengar, S. Thirumalachari, S. Kothandaraman, Experimental study of spray breakup phenomena in small-scale simplex atomizers with and without air swirl, At. Sprays 28 (4) (2018) 299–320.

[24] G. Vignat, Dynamique de l'injection et de la combustion dans des flammes de spray swirlées et couplage azimutal dans les foyers annulaires, 2020, Université Paris-Saclay.

[25] K. Prieur, Dynamique de la combustion dans un foyer annulaire multi-

injecteurs diphasique, 2017, Université Paris-Saclay.
[26] G. Vignat, D. Durox, K. Prieur, S. Candel, An experimental study into the effect of injector pressure loss on self-sustained combustion instabilities in a swirled spray burner, Proc. Combust. Inst. 37 (4) (2018) 5205–5213.
[27] K. Prieur, D. Durox, G. Vignat, T. Schuller, S. Candel, Experimental determinations of flame describing functions of swirling spray flames., in: Colloque INCA, 2017, Châteaufort, France, 2017.
[28] E. Lo Schiavo, D. Laera, E. Riber, L. Gicquel, T. Poinsot, Effects of liquid fuel/wall interaction on thermoacoustic instabilities in swirling spray flames, Combust. Flame 219 (2020) 86–101.
[29] G. Vignat, E. Lo Schiavo, D. Laera, A. Renaud, L. Gicquel, D. Durox, S. Candel, Dynamics of spray and swirling flame under acoustic oscillations : A joint experimental and LES investigation, Proc. Combust. Inst. - in press,doi:https://doi.org/10.1016/j.proci.2020.05.054.
[30] F. Nicoud, F. Ducros, Subgrid-scale stress modelling based on the square of the velocity gradient tensor, Flow, Turbul. Combust. 62 (3) (1999) 183–200.
[31] O. Colin, M. Rudgyard, Development of high-order taylor-galerkin schemes for les, J. Comput. Phys. 162 (2) (2000) 338–371.
[32] T. J. Poinsot, S. Lele, Boundary conditions for direct simulations of compressible viscous flows, J. Comput. Phys. 101 (1) (1992) 104–129.
[33] M. D. Paulhiac, B. Cuenot, E. Riber, L. Esclapez, S. Richard, Analysis of the spray flame structure in a lab-scale burner using Large Eddy Simulation and Discrete Particle Simulation., Combust. Flame 212 (2020) 25–38.
[34] H. Yamashita, M. Shimada, T. Takeno, A numerical study on flame stability at the transition point of jet diffusion flames, Symp. Combust. 26 (1) (1996) 27–34.
[35] B. Abramzon, W. Sirignano, Droplet vaporization model for spray combustion calculations, Int. J. Heat Mass Tran. 32 (9) (1989) 1605–1618.
[36] G. Chaussonnet, O. Vermorel, E. Riber, B. Cuenot, A new phenomenological model to predict drop size distribution in large-eddy simulations of airblast atomizers, Int. J. Multiph.Flow 80 (2016) 29–42.
[37] J. Reveillon, L. Vervisch, Analysis of weakly turbulent dilute-spray flames and spray combustion regimes, J. Fluid Mech. 537 (2005) 317–347.
[38] T. Poinsot, D. Veynante, Theoretical and numerical combustion, RT Edwards, Inc., 2005.
[39] A. Tyliszczak, D. E. Cavaliere, E. Mastorakos, LES/CMC of blow-off in a liquid fueled swirl burner, Flow, Turbul. Combust. 92 (1-2) (2014) 237–267.
[40] P. J. Schmid, Dynamic mode decomposition of numerical and experimental data, J. Fluid Mech. 656 (2010) 5–28.
[41] F. Richecoeur, L. Hakim, A. Renaud, L. Zimmer, DMD algorithms for experimental data processing in combustion, in: Proceeding of the 2012 Summer Program, Center for Turbulence Research, Stanford University, 2012, pp. 459–468.
[42] L. Magri, M. P. Juniper, J. P. Moeck, Sensitivity of the Rayleigh criterion in thermoacoustics, J. Fluid Mech. 882 (2020) 1–5.
[43] L. Rayleigh, The explanation of certain acoustical phenomena, Roy. Inst. Proc. 8 (1878) 536–542.
[44] G. Tissot, L. Cordier, N. Benard, B. R. Noack, Model reduction using Dynamic Mode Decomposition, Comptes Rendus Mécanique 342 (6) (2014) 410–416.
[45] S. Klus, P. Koltai, C. Schütte, On the numerical approximation of the perron-frobenius and koopman operator, arXiv preprint arXiv:1512.05997.

View publication stats